RESEARCH ARTICLE | FEBRUARY 07 2025

Liquid metal droplet generation based on T-junction microchannels

Yunfan Lv; Bowen Li; Shibo Gao; Jan G. Korvink ; Yongbo Deng

Physics of Fluids 37, 022016 (2025)
https://doi.org/10.1063/5.0253098

Physics of Fluids ARTICLE pubs.aip.org/aip/pof

Liquid metal droplet generation based on T-junction microchannels

Cite as: Phys. Fluids **37**, 022016 (2025); doi: 10.1063/5.0253098
Submitted: 14 December 2024 · Accepted: 10 January 2025 ·
Published Online: 7 February 2025 · Corrected: 19 February 2025

Yunfan Lv,[1,2,3] Bowen Li,[1,3] Shibo Gao,[1,2,3] Jan G. Korvink,[4,a)] and Yongbo Deng[4,a)]

AFFILIATIONS

[1]Changchun Institute of Optics, Fine Mechanics and Physics (CIOMP), Dongnanhu Road 3888, Changchun 130033, China
[2]University of Chinese Academy of Sciences, Beijing 100039, China
[3]State Key Laboratory of Advanced Manufacturing for Optical Systems, Dongnanhu Road 3888, Changchun 130033, China
[4]Institute of Microstructure Technology (IMT), Karlsruhe Institute of Technology (KIT), Hermann-von-Helmholtzplatz 1, Eggenstein-Leopoldshafen 76344, Germany

[a)]**Authors to whom correspondence should be addressed:** yongbo.deng@kit.edu and jan.korvink@kit.edu

ABSTRACT

Galinstan liquid metal remains liquid at room temperature and exhibits unique physical properties including fluidity and high electrical conductivity, and its manipulation is a subject of extensive research interest. In contrast to existing control methods, such as electric and magnetic fields, we focus on a novel and efficient approach based on generating liquid metal droplets through microchannels. The present investigation mainly deals with generating liquid metal droplets through establishing a two-dimensional computational model based on the phase-field method for the droplet microfluidics in a T-junction structure. To enhance its performance, a constraint structure is added to expand the adjustment range of droplet formation. The constraint structure and increasing flow rate enhance the viscous shear effect, which reduces the droplet formation length and increases the generation frequency. Polymethyl methacrylate and pressure-sensitive adhesive are laser-cut to fabricate the microchannels. A peristaltic pump is utilized as the driving device, and a high-speed camera is employed to record the liquid metal droplet formation process. Both reducing the constraint ratio and increasing the flow ratio result in accelerated shear rate and increased droplet formation frequency, which is consistent with the simulation results. In experiments, the constraint structure enhanced the viscous shear effect, and relocation of the fracture location was observed. In addition, the high surface tension and inertia of the liquid metal released energy during droplet breakup, leading to noticeable oscillation and deformation of the droplet. Both the simulation and experimental results provide guidelines for the application of liquid metal generation in reconfigurable metasurfaces.

I. INTRODUCTION

Gallium-indium-tin (Galinstan) is a eutectic alloy composed of gallium, indium, and tin, and has a low melting point that allows it to remain liquid at room temperature. Galinstan is composed of 68.5% gallium, 21.5% indium, and 10.0% tin. The brilliant properties of this alloy, including fluidity, high electrical and thermal conductivity, stretchability, self-healing ability, biocompatibility, and recyclability, make this suitable for an extensive range of applications.[1] However, unlike mercury, this liquid metal (LM) alloy is much safer due to its low toxicity and negligible vapor pressure.[2] The unique physical properties of Galinstan have attracted considerable attention from researchers. The injection of liquid metals into microfluidic structures has been broadly utilized in patterning and encapsulating highly deformable and reconfigurable electronic devices, including electrodes,[3] sensors,[4] antennas,[5,6] and interconnects.[7] To effectively manipulate this liquid metal, various techniques have been developed, including the use of electric fields,[8,9] magnetic fields,[10] electrochemical reactions,[11] ultrasonic vibrations,[12] and electrochemistry.[13] Uniformly sized LM droplets can be assembled into periodic structures and show good prospects for electromagnetic applications, such as wireless RF resonators and reconfigurable optical diffraction gratings. Another distinctive feature of Galinstan is the rapid formation of a thin, self-limiting, atomic-scale layer of gallium oxide on the surface upon exposure to oxygen. This oxide layer adheres to surfaces and could hinder mobility. The addition of an acidic or alkaline solution ruptures the oxide layer, restoring the original surface tension and fluidity.[14] Unlike common aqueous-phase or oil-phase fluids, LM consisting of molten metal atoms is essentially characterized by high density and large surface

tension. As a result, splitting a large mass of LM into uniform, micro-sized droplets remains a noticeable challenge.

Microdroplet technology is a micro-technology that is based on the interaction between flow shear and surface tension to split and separate a continuous fluid into discrete droplets at the micro-/nanometer scales. This approach offers advantages such as rapid droplet generation, high throughput, and precise control of droplet size. The droplet generation approaches can be divided into two main categories based on their specific energy consumption: passive and active droplet generators. Passive droplet generators rely on the hydrodynamic pressure of the flow without external energy input, whereas active droplet generators use external power sources to generate droplets. The primary passive generation approaches include T-junction,[15–17] cross-junction,[18,19] and flow-focusing techniques.[20,21] Generally, active generation approaches utilize piezoelectric field,[22] ultrasonic field,[23] electric field variation,[24] and magnetic fields.[25] However, the dynamics of flow-focusing have been mainly examined via model systems for water and oil, with relatively less research on the mechanism of LM droplet generation. Although the viscosity of metals is similar to water, LM possesses several unique properties, including high interfacial tension and high density relative to water. In recent years, microfluidic tunable capacitors, which use fluid displacement of a high-dielectric fluid to alter capacitance, have demonstrated large linear tuning ranges.[26,27] Koo[27] fabricated the LM droplet switch to achieve a turn-on loss of <4 dB and a turn-off loss of <18 dB across a frequency range of 4–15 GHz by changing the position of a liquid metal droplet. However, most existing approaches rely on one-time reconfiguration, making linear control challenging. Therefore, investigations on the generation of liquid metal droplets via microfluidics have been motivated and initiated to enhance the controllability of LM droplets.

To investigate the details of the LM droplet generation process, this paper employs appropriate simulations to model droplet generation and combines them with experimental verification to examine its generation mechanism. Studies of droplet generation have been the focus of many researchers in microfluidics. The similarities and physical principles underlying various techniques for droplet generation have also been extensively investigated.[28] This phenomenon involves the continuous and stable formation of droplets by extruding and shearing two immiscible phases in a microchannel.[29] Tan *et al.*[30] fabricated a microfluidic device that was capable of controlling droplet volume by adjusting the flow rate. Baroud *et al.*[31] explored the main physical factors involved in the generation of oil–water droplets and demonstrated that the flow and pressure fields at the interface play a crucial role in their overall physical and mechanical behavior. Researchers have experimentally investigated the generation and control of droplets and have also employed numerical models to methodically examine the droplet formation process to further understand the generation mechanism. To this end, computational fluid dynamics (CFD), which mainly works based on mathematical models and numerical simulations, has been extensively employed to analyze the properties of fluid flows. Until now, various models have been utilized to explore the behavior of two-phase fluid flows and reveal the dynamic mechanisms of such systems, including the volume-of-fluid (VOF) method,[32] the level-set method,[33] and the phase-field method.[34] Sontti and Atta[35] developed a numerical model based on the VOF approach to study the droplet generation process of non-Newtonian fluids and the factors affecting it, including flow rate and interfacial tension. Jangir and Jana[36] simulated the generation and breakup of droplets using a two-phase conservative level-set method, observing the flow patterns and droplet splitting behaviors. Existing research on microdroplet generation has mainly focused on oil and water phases, and extensive work has summarized the effective factors and principles governing droplet generation, providing a valuable reference for the generation of LM droplets. However, in addition to mobility, LMs are quite different from oil and water phases. Their high surface free energy enlarges the interfacial tension, which makes the formation of discrete droplets more difficult, while their density is 6.43 times that of water, which gives them more inertia in the flow process. When using microchannels to generate LM droplets, it is important to consider whether the difference in physical properties leads to a distinct generation pattern from oil–water droplets. Therefore, it is necessary to examine the generation mechanism and specific patterns of LM droplets in microchannels.

Researchers have experimented with and explored the use of flow control techniques to produce LM droplets. Hutter *et al.*[37] generated LM droplets in a microfluidic device and identified channel size and flow rate as the key factors affecting the droplet shape. Through simulation and experiments, Gol *et al.*[38] produced LM droplets in glycerol, then laterally transferred them into a NaOH solution to achieve separation. Tian *et al.*[39] utilized a microfluidic chip to produce LM droplets and applied an electric field to sort droplets of various sizes. He *et al.*[40] fabricated a coaxial microfluidic device by 3 D printing that enabled the generation of LM droplets in the range of 650 to 1900 μm. Previous research demonstrated the feasibility of producing LM droplets using microfluidic chips. However, the physical properties of LM differ significantly from those of oil and water phases, and few studies have examined the mechanisms of LM droplet generation through simulation. Furthermore, comprehensive summaries of the governing principles and detailed descriptions of the phases involved in the droplet generation process are insufficient. To achieve high-precision generation of LM droplets and their control, further investigation of their generation principles and processes is necessary. The phase-field approach, which is commonly employed to simulate two-phase flow, offers advantages such as accurate interface tracking and high numerical stability.[41] Therefore, we herein use the phase-field model to simulate the droplet generation process and investigate its kinetic mechanisms. Based on these simulations, we establish a platform for studying the generation process and, through experimental observations, systematically analyze the LM droplet generation process, summarize the governing principles, and focus on the analysis of specific phenomena observed during droplet generation.

The structure of this paper is as follows. Section II describes the process of establishing the microchannel model and calculating the droplet generation simulation. Section III presents the experimental process of LM droplet generation and discusses the results. Section IV summarizes the key findings of the present work.

II. MODELING AND SIMULATION

Cross-flow is widely utilized for droplet generation. In these configurations, the dispersed phase is pinched and necked by the viscous shear of the continuous phase. When the shear force exceeds the critical surface tension, the dispersed phase breaks up and forms droplets that are suspended in the continuous phase. In cross-flow geometries, the dispersed-phase and continuous-phase fluids meet at an angle. This is usually implemented as a T-junction, as shown in Fig. 1, where

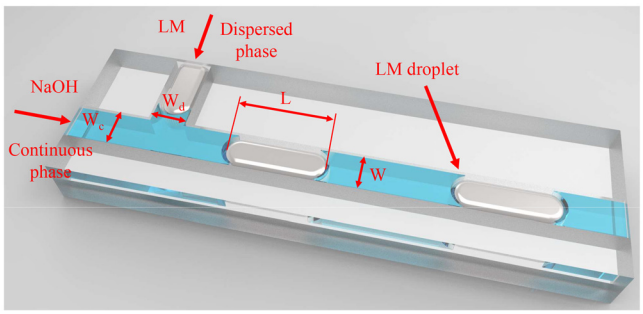

(a)

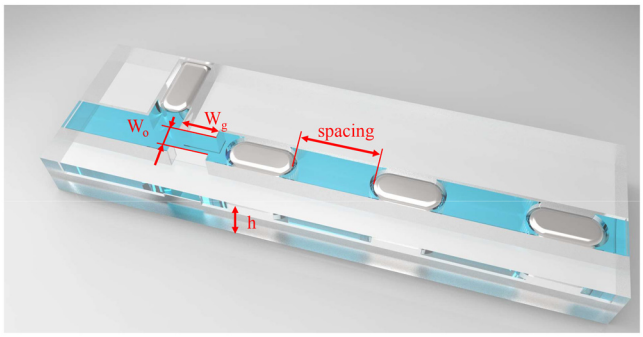

(b)

FIG. 1. Schematic diagram of the microchannel structure: the microchannel consists of dispersed channel, continuous channel, and main channel, where the dispersed channel is perpendicular to the continuous channel and the main channel: (a) microchannel without a constraint structure and (b) microchannel with the constraint structure.

the two fluids intersect at a 90-degree angle, and the dispersed phase is truncated into separate droplets near the junction.

A schematic representation of the channel structure includes a dispersed channel, a continuous channel, and a main channel. The dispersed channel is perpendicular to both the continuous channel and the main channel. Figure 1 illustrates structure of the droplet generation microchannel. The main geometric parameters of such a section are as follows: the width of the dispersed channel ($W_d = 2$ mm), the width of the continuous channel ($W_c = 2$ mm), the width of the main channel ($W = 2$ mm), and the height of the microchannel ($h = 1.5$ mm).

In this case, LM as part of the generated droplets, serves as the dispersed phase, whereas a 1% concentration of NaOH solution is utilized as the continuous phase to remove the oxide layer and protect the LM. The droplet length (L) is measured by drawing a horizontal reference line in the middle of the main channel. The length was defined as the distance from the rear to the front of the droplet after reaching a steady state. Similarly, the droplet spacing was defined as the distance between the tail of the leading droplet and the front of the trailing droplet. In all cases, the average droplet length of the droplets in the microchannel is determined after reaching a steady-state droplet formation. The droplet generation frequency is estimated based on the time required for two consecutive drops to form during stable droplet formation. To facilitate uniform evaluation, the dimensionless constraint ratio, W_r, is defined as the ratio of the main channel width to the constraint width ($W_r = W_o/W$), and the flow ratio is defined as the ratio of the continuous-phase flow rate (Q_c) to the dispersed-phase flow rate (Q_d), represented as the dimensionless flow ratio Q_r ($Q_r = Q_c/Q_d$).

A two-dimensional model based on the horizontal cross section of the channel could precisely simulate the LM droplet generation process and calculate the flow process and the flow velocity distribution of the dispersed phase in the microchannel. Such a model aims to help in analyzing the contribution of forces in the droplet generation process and summarizing the changes of pressure and viscous forces in the shear force during the droplet generation process, as well as the main forces that truncate the droplets under different conditions. Both LM and NaOH solution were assumed to be incompressible, immiscible, and Newtonian. The main governing equations exploited to describe the flow behavior in the microchannel were the Navier–Stokes equation, establishing the relationship between the momentum and shear forces of the dispersed phase and the continuous phase. In addition, the continuity equation was employed to describe the flow in the control volume, where the density and dynamic viscosity of the NaOH solution and LM remain constant in this model,

$$\rho\left[\frac{\partial v}{\partial t} + (v\cdot\nabla)v\right] = -\nabla p + \nabla\cdot K + G\nabla\phi + \rho\mathbf{g}, \quad \text{in}\,\Omega$$
$$\nabla\cdot v = 0, \quad \text{in}\,\Omega, \tag{1}$$

where $\vec{v} = (u, v, w)$ is the velocity vector, ∇p and ρ in order represent the pressure gradient and the density of the fluid, which describes the rate of change of momentum. On the right side of the equation, the effects of pressure forces are given. The term $K = \mu(\nabla\vec{v} + (\nabla\vec{v})^T)$ denotes the shear stress tensor, which provides the viscous drag force. Considering the microchannel dimensions, gravitational acceleration is neglected due to the scale of the model, and the surface tension at the interface of the two-phase fluid is treated as the main force. This surface tension is included as an additional force, given by $G\nabla\phi$, where G denotes the chemical potential, calculated as follows:

$$G = \lambda\left[-\nabla^2\phi + \frac{\phi(\phi^2-1)}{\varepsilon^2}\right], \tag{2}$$

where λ represents the mixing energy density of the interface, and ε is the interfacial thickness between the two-phase liquids.

Through the current investigation, a phase-field model based on the Cahn–Hilliard equation was employed to simulate the LM droplet generation in the T-junction microfluidic geometry. This model is capable of describing the diffuse interface between the LM phase and the NaOH phase. The fourth-order Cahn–Hilliard equation, composed of two second-order partial differential equations, is described in the following form:

$$\frac{\partial\phi}{\partial t} + \vec{u}\nabla\phi = \nabla\cdot\frac{\gamma\lambda}{\varepsilon^2}\nabla\psi, \quad \text{in}\,\Omega, \tag{3}$$

$$\psi = -\nabla\cdot\varepsilon^2\nabla\phi - (\phi^2-1)\phi, \quad \text{in}\,\Omega, \tag{4}$$

where ϕ represents the volume fraction of each phase as described in the following:

$$\phi = \begin{cases} -1 \\ -1 < \phi < 1 \\ 1. \end{cases} \tag{5}$$

The phase-field variable ϕ varies from -1 to 1. In the case of $\phi = -1$, the unit point belongs to the LM phase, whereas for the case

TABLE I. Physical properties of the selected liquids.

Description	Liquid	Density (kg/m^3)	Dynamic viscosity (Pa · s)
Dispersed phase	LM	6423	2.4×10^{-3}
Continuous phase	NaOH	1000	1.95×10^{-3}

of $\phi = 1$, it belongs to the NaOH phase. The region with ϕ between -1 and 1 represents the interface zone located between the two phases. Therefore, the volume fractions of the fluids (LM and NaOH) can be computed as

$$V_f = \frac{1+\phi}{2}, \tag{6}$$

where $\gamma = \chi\varepsilon^2$ represents the phase-field mobility, and χ is a mobility tuning parameter that is proportional to the characteristic velocity and inversely proportional to the surface tension. The ε determines the timescale of Cahn–Hilliard diffusion and is typically set to half of the maximum mesh size in the computational domain where the interface passes, in order to ensure computational accuracy and convergence.

Thus, the density and viscosity of the entire computational domain can be treated as those of an effective fluid with averaged physical properties, which were obtained using the following expressions:

$$\rho = \phi\rho_c + (1-\phi)\rho_d, \tag{7}$$

$$\mu = \phi\mu_c - (1-\phi)\mu_d. \tag{8}$$

The commercial finite element software COMSOL Multiphysics was effectively utilized to establish a two-dimensional model to simulate the droplet generation process. A two-dimensional model based on the horizontal cross section of the channel can accurately simulate the LM droplet generation process and calculate the flow process and the velocity distribution of the dispersed-phase flow in the microchannel, which helps to analyze the contribution of forces in the channel. The droplet generation process summarizes the changes of pressure and viscous forces in the shear force during the droplet generation process, as well as the main forces that shorten the droplets under different conditions. For the characteristic length of the above-mentioned microfluidic system, the following main items are taken into account: the laminar flow two-phase phase-field model under the CFD module for simulation, LM for the dispersed phase, and 1% NaOH for the continuous phase. The values of the physical properties used for the calculation are presented in Table I. The contact angle of LM in NaOH was measured to be 133°, and the interfacial tension was set to be 480 mN/m. The entries of the discrete phase and continuous phase were set as the velocity inlet, and the outlet is the zero pressure condition. The 2 D simulation mode and initial boundary conditions are illustrated in Fig. 2. The dispersed-phase inlet is located at the top, with $\phi = -1$ in the dispersed-phase channel, whereas the continuous-phase inlet is located on the left, with the continuous-phase channel and the main channel initially set as $\phi = 1$. The width of the microchannel model matches the actual channel width, with the dispersed- and continuous-phase channels expanded to allow for fully developed flow. The main channel is designed with sufficient length to ensure that droplets are generated and fully enter the stabilization stage. A mesh independence study was performed to determine the appropriate number of meshes while ensuring computational convergence. Four simulations were performed using different numbers of non-uniform computational grids: 8619, 11 960, 24 867, and 59 179. The obtained results indicate that sufficient computational accuracy can be achieved with 24 867 grids.

The study of the effect of the constraint width on the LM droplet generation helps to understand the influence of the constraint structure on the droplet generation process. To examine the effect of the constraint width on the droplet formation, the flow rate and fluid

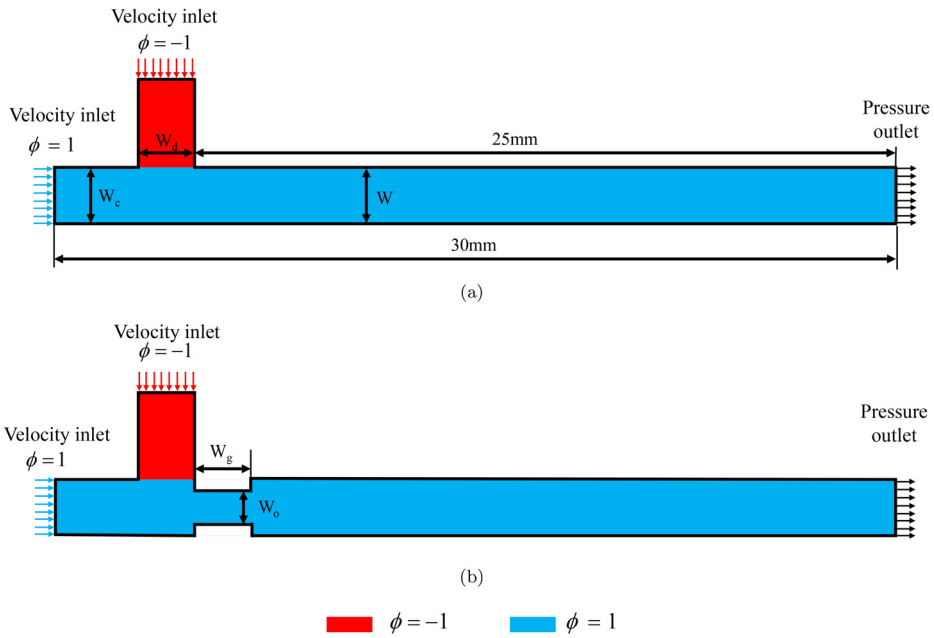

FIG. 2. Sketch for the boundary conditions of the 2 D simulation model: (a) microchannel without a constraint structure and (b) microchannel with the constraint structure.

properties were kept constant. As illustrated in Fig. 3, the time evolution of the droplet formation process was analyzed for a deeper understanding of the numerical results and their associated trends. The process of LM droplet generation can be divided into distinct stages, filling, necking, detachment, and lagging, corresponding to the phases I, II, III, and IV in Fig. 3. During the filling stage, the dispersed-phase front expands while remaining spherical due to interfacial tension. As the volume of the dispersed phase increases and the pressure of the continuous phase is applied, the droplet grows and moves in the direction of the main channel. In the necking stage, a shear ramp, as shown in Fig. 3(a) at 0.10 s, is developed in a standard T-junction channel without necking, driven by the continuous phase pressure. The distance between the shear ramp and the apex of the channel intersection lessens over time. Once the shear force exerted by the pressure at the shear ramp exceeds the interfacial tension, the system enters the detachment stage, where the shear force overcomes the viscosity and interfacial tension in the necking region. The dispersed phase breaks up near the channel intersection and generates separate LM droplets, which is called the lagging stage. Following this, the sharp front of the dispersed phase retracts and forms a rounded interface due to interfacial tension. Meanwhile, the sharp tail of the droplet contracts and, under the combined effect of channel extrusion and interfacial tension, the droplet takes on a rounded-end shape. This evolution mechanism is consistent with the findings of Liu *et al.*[42] and confirms that the physical properties of LM are suitable for use in microfluidic droplet generation devices.

By defining the normalized constraint width W_r as 1 for the non-constraint case, the effect of constraint width on the droplet length and the generation frequency for a fixed operation and flow rate is illustrated in Fig. 4. It is evident that increasing the dimensionless constraint width directly influences the droplet formation. As the constraint width expands from 0.4 to 1, the length of the droplet increases from 3.2 to 6.6 mm, the spacing of the droplet generation cycle extends from 5.5 to 11.7 mm, and consequently, the frequency of generation decreases from 14.28 Hz to 6.67 Hz. This is essentially attributed to the increased shear in the dispersed phase in constraint. In addition, the geometric constraints, together with the increased viscous forces in the continuous phase, contribute to faster droplet generation. The velocity profile at the necking stage, as shown in Fig. 5, reveals a significant increase in velocity in constraint structure. This enhances the viscous shear of the continuous phase, which continues to increase with increasing constraint width W_r. The constraint structure effectively enhances the viscous shear in the continuous phase, leading to shorter droplet generation cycles, increased frequency, and

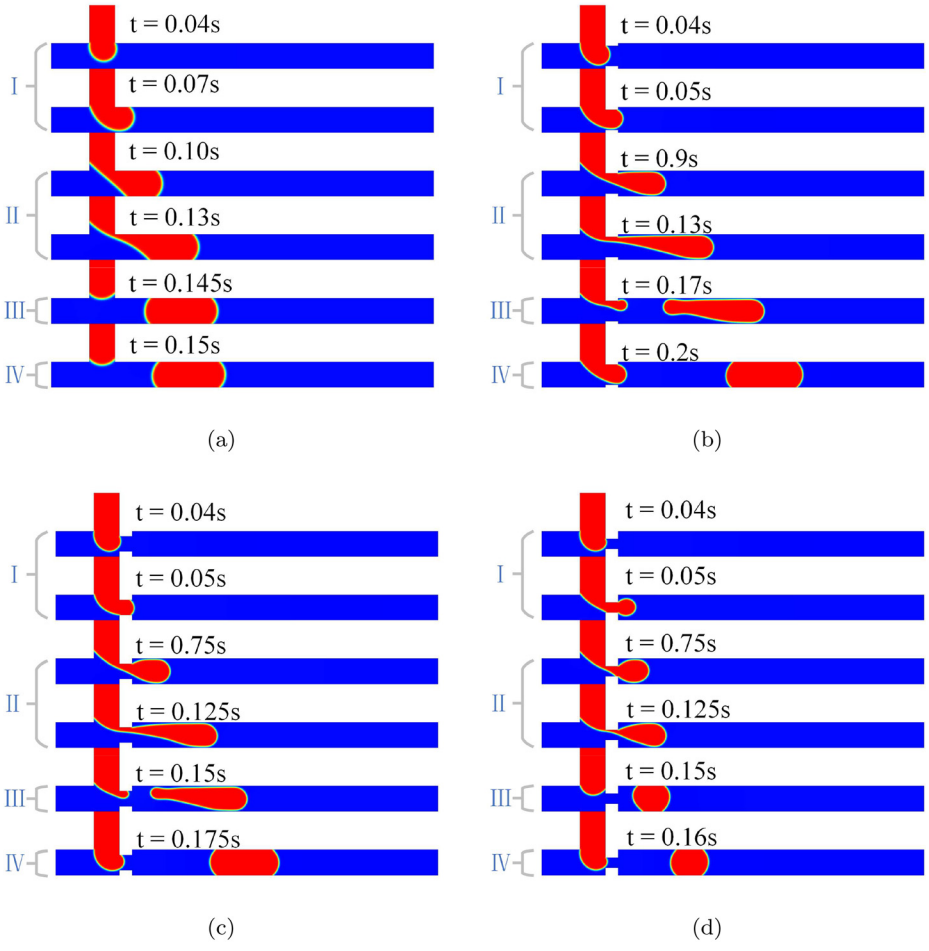

FIG. 3. Droplet generation processes with fixed LM and NaOH flow rate at different dimensionless constraint ratios: (a) $W_r = 1$; (b) $W_r = 0.8$; (c) $W_r = 0.6$; and (d) $W_r = 0.4$.

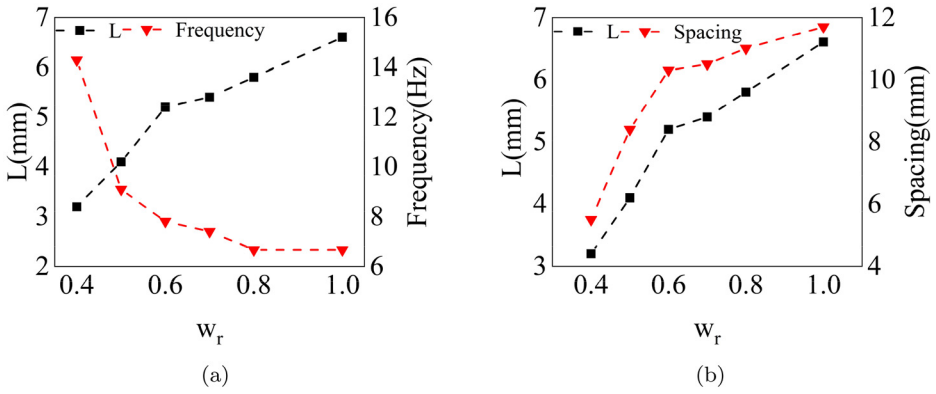

FIG. 4. LM droplet variation under different dimensionless constraint ratios: (a) LM droplet length and generation frequency and (b) LM droplet length and droplet spacing.

reduced droplet length and spacing, assuming that the flow ratio remains constant.

In the current investigation, we are also interested in examining the effect of continuous-phase flow rate on the droplet formation in microchannels with a constant dispersed-phase flow rate, based on the microchannel without constraint structure. The flow ratio Q_r is defined as the ratio of the continuous-phase flow rate to the dispersed-phase flow rate. As demonstrated in Fig. 6, the interfaces of the continuous and dispersed phases move faster with increasing Q_r. In addition, the changing of the angle between the two-phase interfaces and the horizontal plane follows a similar trend, which is mainly ascribed to the growth of the shear effect of the continuous phase. To further recognize the droplet formation process, the droplet parameters were quantitatively analyzed based on Q_r, as shown in Fig. 7. The droplet length reduces 8.6 to 5.6 mm with the increase in Q_r, whereas the droplet generation frequency increases from 4.54 Hz to 7.41 Hz, which is essentially related to a reduction in the droplet generation time. This effect is primarily attributed to the increase in the shear force applied to the LM.

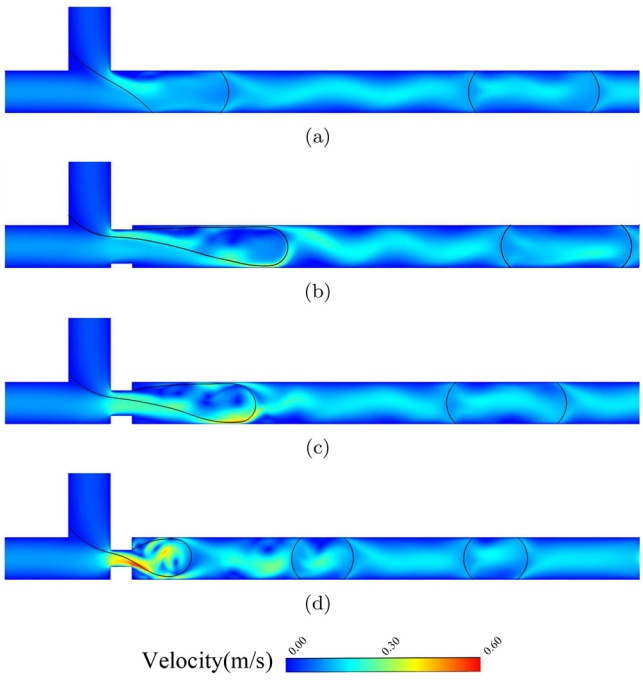

FIG. 5. Velocity distribution in the necking stage of droplet generation at different constraint ratios: (a) $W_r = 1$; (b) $W_r = 0.8$; (c) $W_r = 0.6$, and (d) $W_r = 0.4$.

Figure 8 illustrates the flow velocity distribution during the generation of LM droplets at different flow ratios. As the flow ratio rises, the flow velocity of the continuous phase accelerates, especially before the dispersed phase contacts the lower wall of the main channel during the filling stage. This indicates an increase in the contribution of the viscous shear force of the continuous phase during the shear process. After droplet detachment, the velocity directions of both the continuous and dispersed phases fluctuate in the main channel. The higher the flow ratio, the more pronounced the fluctuation in the flow direction with uneven velocity distribution inside the LM droplet. This is mainly ascribed to the asymmetric structure of the T-junction that produces the droplet and also the high surface free energy of LM caused by its high interfacial tension. The energy fluctuations during the droplet detachment further amplify these flow fluctuations. As the flow ratio increases, the continuous phase is constrained by the shape of the dispersed phase, resulting in an increase in the flow velocity and the generation of velocity components that lead to flow fluctuations.

III. EXPERIMENTS, RESULTS, AND DISCUSSION

The droplet-generating chip materials were selected as polymethyl methacrylate (PMMA) and pressure-sensitive adhesive (PSA): the PMMA sheet was bonded on both sides with PSA as the microfluidic channel layer; the channel fabrication was completed by laser cutting; and the cover plate with holes and connections was bonded to complete the encapsulation, as illustrated in Fig. 9. Based on the boundary conditions of the numerical model and the size of the droplet generator chip, the flow ranges of the dispersed phase (LM) and the continuous phase (NaOH) were appropriately evaluated. Two Lead Fluid BT103S peristaltic pumps were selected as the driving elements. The density, viscosity, and other physical properties of the liquids affect the flow rate of the peristaltic pump. To minimize the pulsation of the flow rate, the peristaltic pumps were equipped with pulse dampers. The flow rate of LM and NaOH solution pumps should be suitably calibrated, and the obtained results are presented in Fig. 10(a). A FASTCAM Mini UX100 high-speed camera was utilized to record the droplet generation process with a frame rate of 1000 fps to meet the

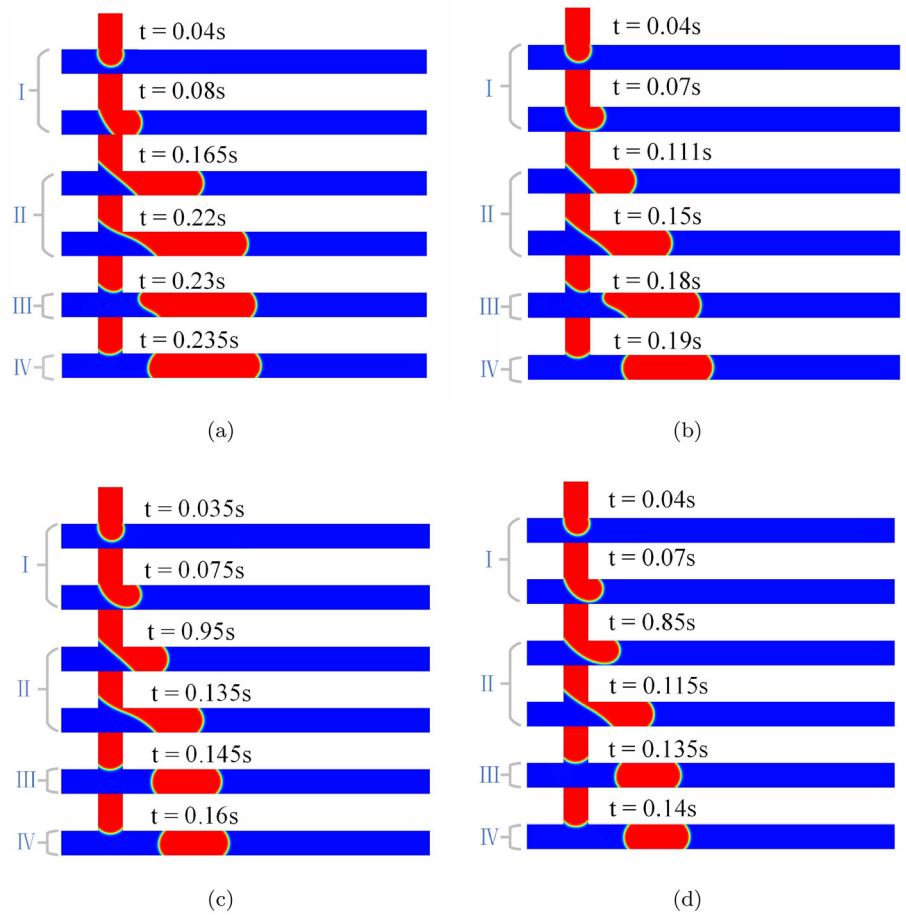

FIG. 6. Droplet generation at different flow ratios in the microchannel without the constraint structure: (a) $Q_r = 1$; (b) $Q_r = 1.5$; (c) $Q_r = 2$, and (d) $Q_r = 2.5$.

experimental recording requirements. The setup of the designed experimental investigation has been demonstrated in Fig. 10(b).

Based on the simulation results, the flow ratio has been fixed to perform the droplet generation experiment under varying constraint ratios. Figure 11 illustrates the LM droplet generation process at a constant flow rate with various dimensionless constraint ratios. It can be clearly seen that with the lessening of W_r from 1 to 0.4, the droplet length is substantially shortened from 6.48 to 3.44 mm, the distance between the droplets is reduced from 5.97 to 3.20 mm, and the generation frequency is increased from 5.21 Hz to 10.99 Hz, which is consistent with the two-dimensional simulation results. In Fig. 11(a) at $t = 0.390$ s, the shear surface appears curved, which differs from the two-dimensional simulation results. This difference is mainly related to the fact that the actual channel inherently possesses a three-

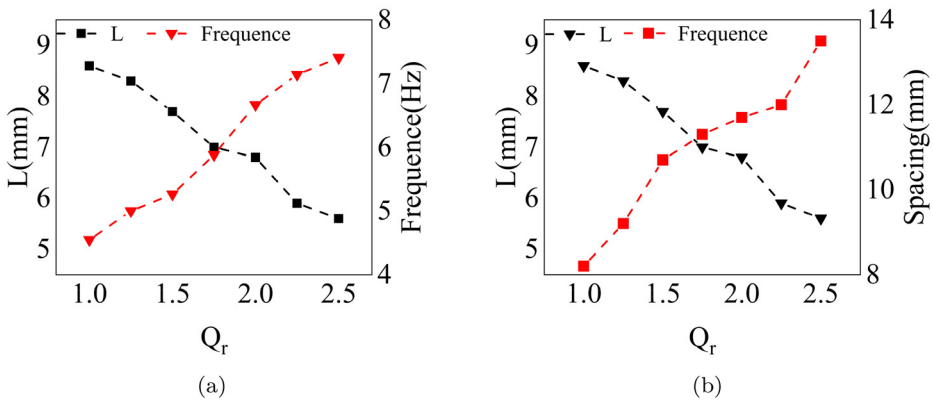

FIG. 7. LM droplet variation process under different flow ratios: (a) LM droplet length and generation frequency and (b) LM droplet length and droplet spacing.

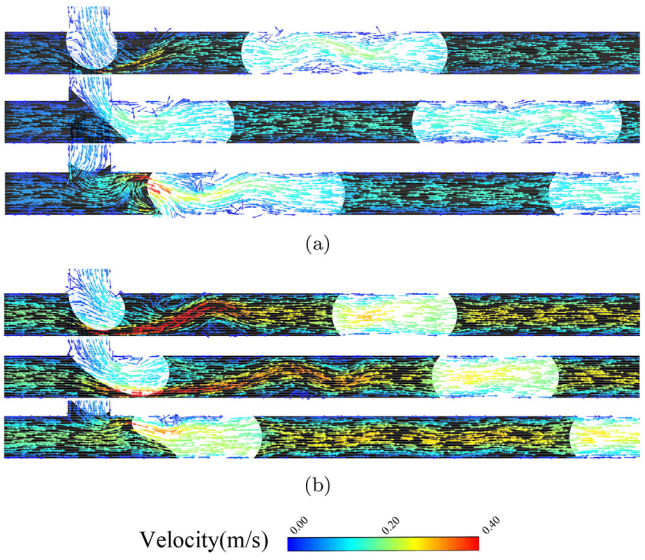

FIG. 8. Flow velocity distributions of filling, necking, and detachment stages at different flow ratios: (a) $Q_r = 1$ and (b) $Q_r = 2$.

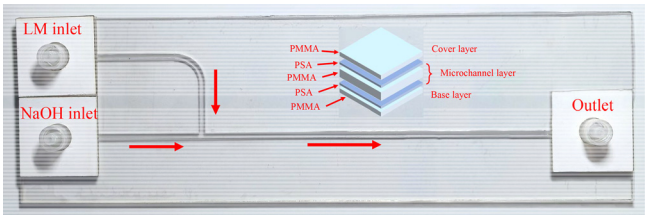

FIG. 9. Microchannel fabricated by laser cutting process of PMMA and PSA.

dimensional structure. In the rectangular microchannel cross section perpendicular to the flow direction, the LM does not completely fill the entire channel. Due to the effect of interfacial tension, the dispersed fluid still passes through it, which leads to some differences between the two-dimensional model and the actual flow state. The droplet length was measured using a 1 mm square mark on the chip, and the average length of the LM droplets generated at various times under uniform conditions was calculated. The final frame before LM droplet detachment was considered as the reference moment to calculate the time and frequency of droplet generation, as shown in Fig. 12. This phenomenon also indicates that the shear force of the continuous phase plays a decisive role in the formation of LM droplets.

The most direct effect of the dimensionless constraint ratio was observed in the change of the channel's shape, which constrains the shape of the dispersed phase as it passes through the continuous phase. As illustrated in Fig. 11, by decreasing the constraint ratio, the dispersed phase fills the channel earlier, allowing the shearing dominated by the pressure of the continuous phase to occur earlier. At the same time, due to the constant flow rate and incompressibility of the liquid, the increase in the flow velocity through the constraint structure increases the shearing effect of the continuous phase on the dispersed phase. As shown in Fig. 13, this leads to a shift in the droplet detachment position further downstream. Starting from the dispersed-phase channel, the detachment position extends from 0.76 to 1.38 mm.

With the dispersed-phase pump speed fixed at 30 rpm, the flow ratio was adjusted by varying the speed of the continuous-phase pump. Figure 14 shows the behavior of LM droplet generation as the flow ratio changes in a structure without constraint. As the flow ratio Q_r increases from 1.22 to 2.16, the continuous-phase flow rate increases, enhancing the shear effect on the LM. Consequently, the length of the LM droplets decreases gradually from 8.40 to 4.66 mm, while the spacing between them increases from 5.28 to 9.21 mm. This behavior aligns with the results of the previous simulation, as shown in Fig. 15.

In the experiments, we observed a significant oscillation phenomenon in the tail of the LM droplet after its formation. As demonstrated in Fig. 16, between 0.072 and 0.078 s, the tail of the LM droplet exhibits a clear process of flinging toward the lower wall of the channel before recovering to a stable arc shape after deformation. Simultaneously, surface corrugations are formed on the droplet, propagating from the tail to the front. In Fig. 16 at 0.084 s, the middle part of the droplet appears concave due to these fluctuations. Once the oscillation terminates, the droplet shape stabilizes, allowing the droplet length to be measured. Furthermore, after the LM droplets detach, the head of the dispersed phase exhibits oscillations, as shown in Fig. 16 between 0.072 and 0.078 s, and stabilizes at 0.084 s, which recovers stability earlier than the droplet. The occurrence of this oscillation phenomenon indicates

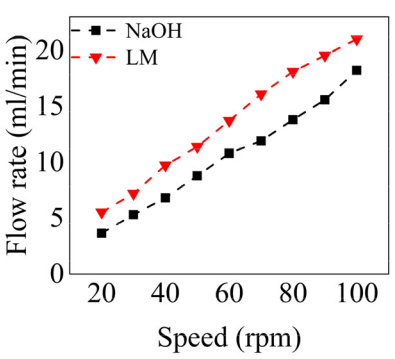

(a)

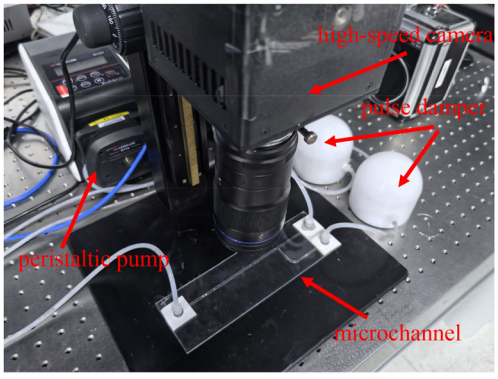

(b)

FIG. 10. (a) Flow rate variation of LM and NaOH along with the pump speed; (b) experimental platform.

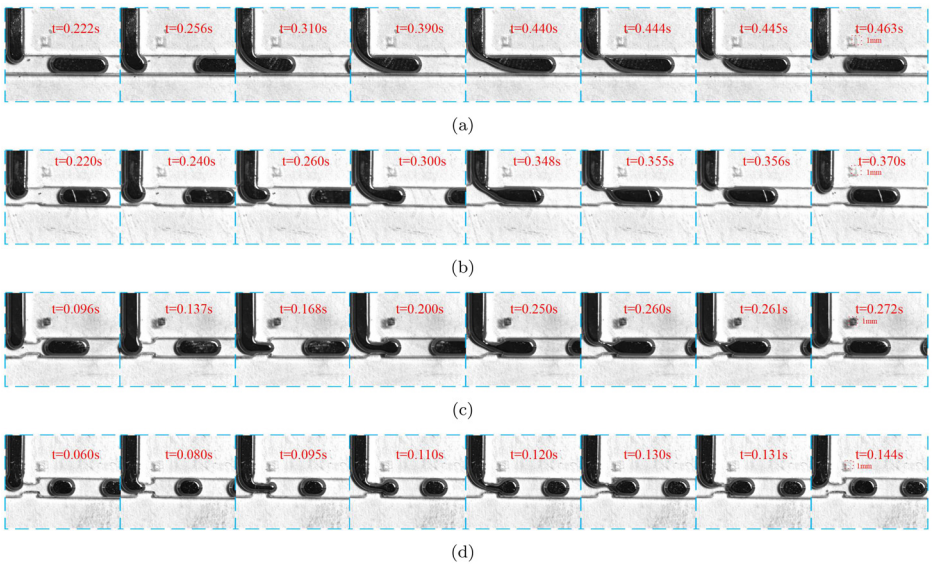

FIG. 11. Droplet generation processes at different dimensionless constraint ratios: (a) $W_r = 1$; (b) $W_r = 0.8$; (c) $W_r = 0.6$; and (d) $W_r = 0.4$.

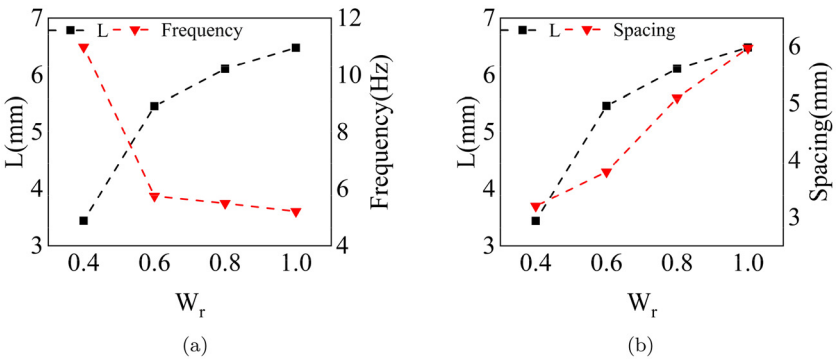

FIG. 12. Experimentally recorded variation along with W_r: (a) LM droplet length and generation frequency and (b) LM droplet length and droplet spacing.

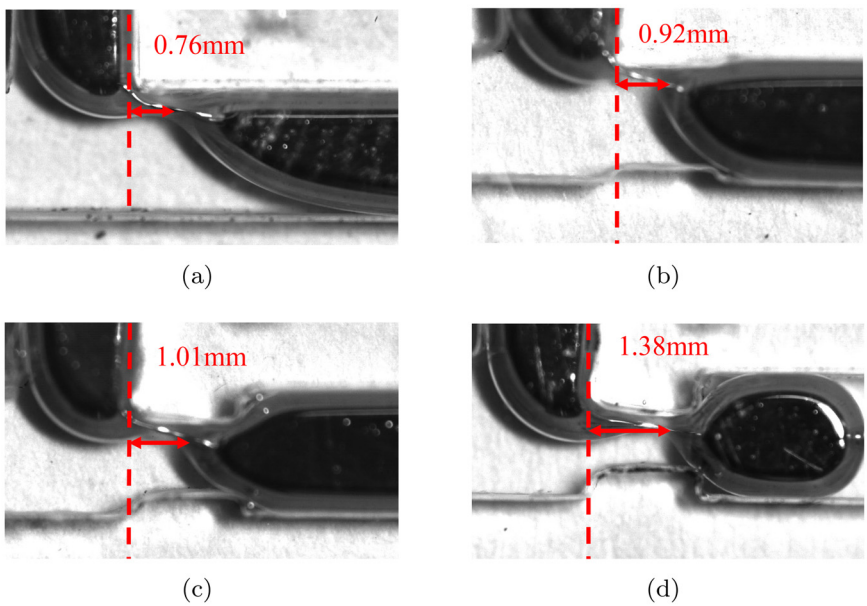

FIG. 13. Location of LM droplet detachment for different dimensionless constraint ratios: (a) $W_r = 1$; (b) $W_r = 0.8$; (c) $W_r = 0.6$; and (d) $W_r = 0.4$.

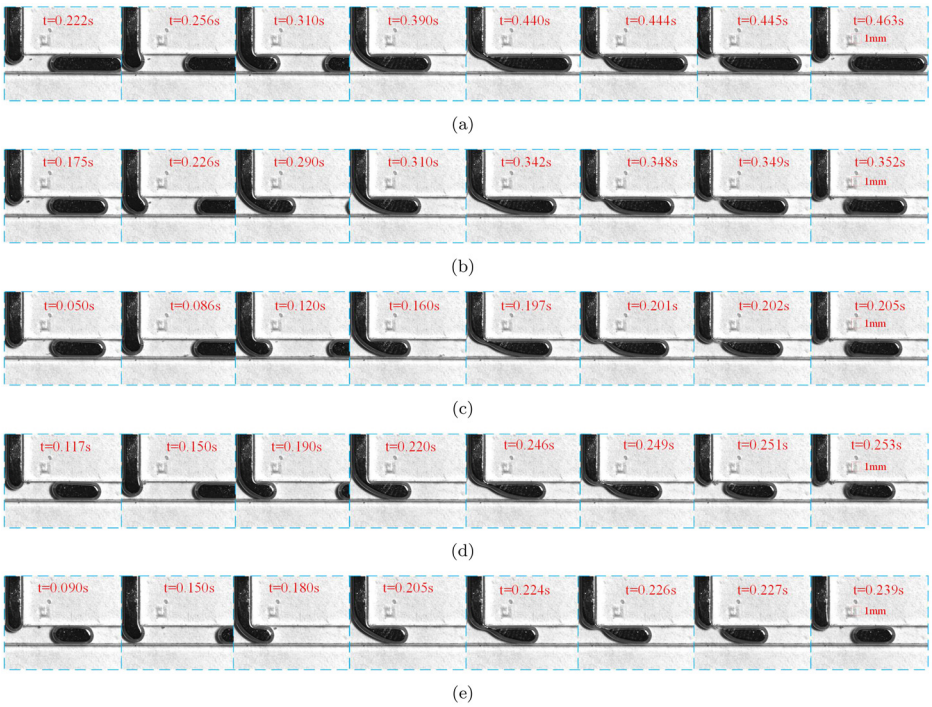

FIG. 14. Droplet generation processes at different flow ratios with dispersed-phase pump speed fixed at 30 rpm: (a) $Q_r = 1.21$; (b) $Q_r = 1.50$; (c) $Q_r = 1.64$; (d) $Q_r = 1.91$; and (e) $Q_r = 2.16$.

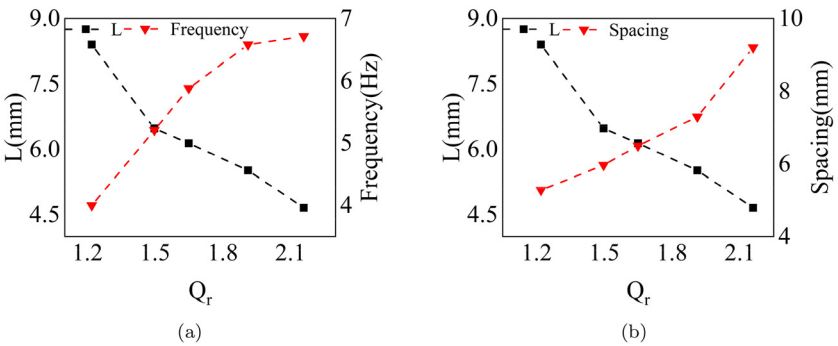

FIG. 15. Experimentally recorded variation along with flow ratio: (a) LM droplet length and generation frequency and (b) LM droplet length and droplet spacing.

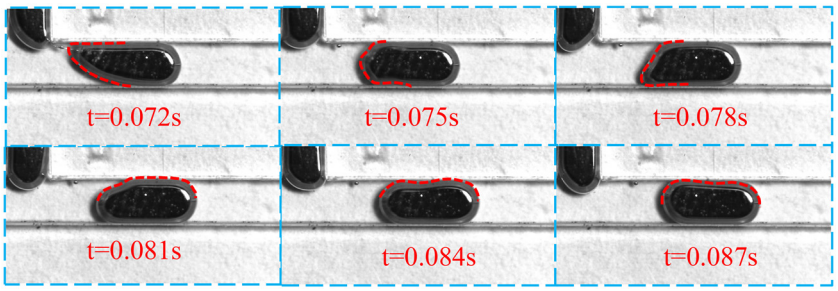

FIG. 16. The droplet breaks up and enters the lagging stage with $Q_r = 2.16$, including the deformation process of the droplet interface.

that the lagging stage is prolonged during the droplet generation cycle. The lagging stage, where the droplet recovers its initial interfacial shape, remarkably overlaps with the LM filling phase at the inlet of the dispersed phase. This phenomenon is essentially attributed to the density and interfacial tension of the LM, which gives it greater inertia and higher interfacial tension compared to typical two-phase fluids. This results in a higher surface free energy, which leads to a more pronounced energy transition during the droplet generation process, and

significant oscillations are observed. This deformation process is also a significant difference between the formation of LM droplets and the oil–water phase.

IV. CONCLUSIONS

In this paper, a two-dimensional phase-field model has been employed to methodically examine the mechanism of LM droplet generation and to use PMMA to fabricate T-junction microchannels to summarize the rules of LM droplet generation. The geometrical constraints of the channel and the ratio of two liquid flow rates are anticipated to play a pivotal role in the droplet generation process and remarkably influence the length of LM drops. To methodically examine this, a two-dimensional droplet generation CFD model is developed based on the phase-field method and is then experimentally validated based on the model calculations. This work demonstrates that LM with high surface tension could generate droplets in T-junction microchannels like other liquids. The LM droplet generation process can be controlled by various conditions, such as structural constraints and flow ratios. These conditions were experimentally confirmed and recorded using a high-speed camera. The effects of the constraint width and the flow velocity of the continuous phase on the length, spacing, and frequency of LM droplet generation are systematically examined in some detail. The obtained results reveal that both the reduction of the constraint width and the increase in the flow ratio lead to an increase in the flow rate of the continuous phase in the channel, which leads to the growth of the viscous shear effect on the discrete phase and accelerates the separation of LM droplets. This crucial conclusion indicates that the control of the viscous shear force on the discrete phase is a determining factor in the formation of LM droplets and provides an effective guideline to achieve more precise control over the droplet formation process. The microchannels were fabricated based on the numerical model, and the experimental results were then compared with the simulations. The Statistical results were in reasonably good agreement with the numerical predictions and confirm the simulation's validity. During long periods of operation, LM droplet generation was maintained with minimal errors between the predicted and observed droplet lengths and generation frequencies.

In experiments, we observed that the detachment position moved forward as the constraint ratio decreased. The constraint structure increased the local flow velocity and increased the shear action of the continuous phase. This increase in viscous shear further shifts the detachment position. This phenomenon strongly supports the conclusion that viscous shear is the determining factor in the formation process of LM droplets. At the same time, the observations reveal that the deformation and fluctuation of the droplet become more pronounced after separation. The lagging stage, during which the droplets transitioned to a steady state, was significantly longer than that predicted by the simulation. Furthermore, the higher surface free energy and higher density of the LM droplet caused its tail to retain considerable kinetic energy after detachment, which is notably different from the behavior of oil–water and other fluids. Our results provide a novel approach for controlling liquid metal and provide insight into the mechanisms and governing laws of LM droplet generation. We construct an experimental setup and perform experimental verification. The results obtained from the simulations, together with the corresponding experimental data, help to ensure the continuous and stable generation of LM droplets over long periods, which has significant applications in scenarios requiring high-throughput, stable LM droplet generation. Therefore, the findings of this study provide valuable guidelines for practical applications of LM, including in flexible sensing, liquid metal metasurface, and flexible electrodes.

ACKNOWLEDGMENTS

This work was supported by the CAS Project for Young Scientists in Basic Research (YSBR-066), the National Natural Science Foundation of China (Grant No. 51875545), the Innovation Grant of Changchun Institute of Optics, Fine Mechanics and Physics (CIOMP), the Science and Technology Development Plan of Jilin Province (Grant No. SKL202302020), an EU2020 FET grant (TiSuMR, 737043), the DFG under grant KO 1883/20-1 Metacoils, funding within their framework of the German Excellence Initiative under grant EXC 2082 "3D Matter Made to Order," and the VirtMat initiative "Virtual Materials Design."

AUTHOR DECLARATIONS

Conflict of Interest

The authors have no conflicts to disclose.

Author Contributions

Yunfan Lv: Conceptualization (equal); Formal analysis (equal); Investigation (equal); Methodology (equal); Validation (equal); Writing – original draft (equal). **Bowen Li:** Formal analysis (equal); Investigation (equal); Methodology (equal); Validation (equal). **Shibo Gao:** Formal analysis (supporting); Investigation (supporting); Methodology (supporting); Supervision (supporting); Validation (supporting). **Jan G. Korvink:** Conceptualization (equal); Supervision (equal). **Yongbo Deng:** Conceptualization (equal); Data curation (equal); Formal analysis (equal); Funding acquisition (equal); Investigation (equal); Methodology (equal); Project administration (equal); Resources (equal); Software (equal); Supervision (equal); Validation (equal); Visualization (equal); Writing – original draft (equal); Writing – review & editing (equal).

DATA AVAILABILITY

The data that support the findings of this study are available within the article and its supplementary material.

REFERENCES

[1]T. Liu, P. Sen, and C.-J. Kim, "Characterization of nontoxic liquid-metal alloy Galinstan for applications in microdevices," J. Microelectromech. Syst. **21**(2), 443–450 (2012).
[2]K. Foremny *et al.*, "Biocompatibility testing of liquid metal as an interconnection material for flexible implant technology," Nanomaterials **11**(12), 3251 (2021).
[3]N. Pekas, Q. Zhang, and D. Juncker, "Electrostatic actuator with liquid metal–elastomer compliant electrodes used for on-chip microvalving," J. Micromech. Microeng. **22**(9), 097001 (2012).
[4]K. Munirathinam *et al.*, "Galinstan-based flexible microfluidic device for wireless human-sensor applications," Sens. Actuators, A **315**, 112344 (2020).
[5]K. N. Paracha *et al.*, "Liquid metal antennas: Materials, fabrication and applications," Sensors **20**(1), 177 (2019).
[6]J.-H. So *et al.*, "Reversibly deformable and mechanically tunable fluidic antennas," Adv. Funct. Mater. **19**(22), 3632–3637 (2009).
[7]S. Erlenbach *et al.*, "Flexible-to-stretchable mechanical and electrical interconnects," ACS Appl. Mater. Interfaces **15**(4), 6005–6012 (2023).

[8]S.-Y. Tang *et al.*, "Electrochemically induced actuation of liquid metal marbles," Nanoscale **5**(13), 5949–5957 (2013).
[9]J. Xie *et al.*, "Modeling and motion control of a liquid metal droplet in a fluidic channel," IEEE/ASME Trans. Mechatron. **25**(2), 942–950 (2020).
[10]X. Li *et al.*, "Programmable digital liquid metal droplets in reconfigurable magnetic fields," ACS Appl. Mater. Interfaces **12**(33), 37670–37679 (2020).
[11]M. Song *et al.*, "Interfacial tension modulation of liquid metal via electrochemical oxidation," Adv. Intelligent Syst. **3**(8), 2100024 (2021).
[12]Z. Li *et al.*, "Ultrasonic cavitation at liquid/solid interface in a thin Ga–In liquid layer with free surface," Ultrason. Sonochem. **71**, 105356 (2021).
[13]J. Han *et al.*, "Exploring electrochemical extrusion of wires from liquid metals," : ACS applied materials interfaces **12**(27), 31010–31020 (2020).
[14]J. W. Boley, E. L. White, and R. K. Kramer, "Mechanically sintered gallium–indium nanoparticles," Adv. Mater. **27**(14), 2355–2360 (2015).
[15]S. K. Jena *et al.*, "Effect of channel width on droplet generation inside T-junction microchannel," Phys. Fluids **35**(2), 022107 (2023).
[16]S. Mehraji and M. Saadatmand, "Flow regime mapping for a two-phase system of aqueous alginate and water droplets in T-junction geometry," Phys. Fluids **33**(7), 072009 (2021).
[17]K. He *et al.*, "Study on the self-adaptive process of droplet traffic to a perturbation of flow resistance at the arms of a micro-T-junction," Phys. Fluids **36**(2), 022013 (2024).
[18]R. Lanfranco *et al.*, "Phantom membrane microfluidic cross-flow filtration device for the direct optical detection of water pollutants," Sens. Actuators, B **257**, 924–930 (2018).
[19]L. Duan *et al.*, "Polymeric droplet formation and flow pattern evolution in capillary microchannels: Effect of fluid elasticity," Phys. Fluids **36**(3), 033112 (2024).
[20]M. Fatehifar *et al.*, "A numerical analysis of particle encapsulation in a flow-focusing droplet generation device," Phys. Fluids **35**(11), 113317 (2023).
[21]Y. Pang *et al.*, "Interface coupling and droplet size under various flow-focusing geometry dimensions in double emulsion formation," Phys. Fluids **35**(12), 122016 (2023).
[22]S. Wang, Y. Zhong, and H. Fang, "Deformation characteristics of a single droplet driven by a piezoelectric nozzle of the drop-on-demand inkjet system," J. Fluid Mech. **869**, 634–645 (2019).
[23]A. D. Ledbetter *et al.*, "Tuning the coupled-domain response for efficient ultrasonic droplet generation," IEEE Trans. Ultrason. Ferroelectr. Freq. Control **65**(10), 1893–1904 (2018).
[24]Q. Wang *et al.*, "Manipulation of a nonconductive droplet in an aqueous fluid with AC electric fields: Droplet dewetting, oscillation, and detachment," Langmuir **37**(41), 12098–12111 (2021).
[25]V. Babulalji Varma *et al.*, "Droplet merging on a lab-on-a-chip platform by uniform magnetic fields," Sci. Rep. **6**(1), 37671 (2016).
[26]S. O. Choi *et al.*, "A tunable capacitor using an immiscible bifluidic dielectric," in *2004 IEEE MTT-S International Microwave Symposium Digest (IEEE Cat. No. 04CH37535)* (IEEE, 2004), Vol. 2, pp. 873–876.
[27]D. T. McCormick, Z. Li, and N. Tien, "Dielectric fluid immersed MEMS tunable capacitors," In *IEEE MTT-S International Microwave Symposium Digest* (IEEE, 2003), Vol. 1, pp. 495–498.
[28]R. Seemann *et al.*, "Droplet based microfluidics," Rep. Prog. Phys. **75**(1), 016601 (2012). Doi:. url:.
[29]Y. Ding, P. D. Howes, and A. J. deMello, "Recent advances in droplet microfluidics," Anal. Chem. **92**(1), 132–149 (2020).
[30]Y.-C. Tan, V. Cristini, and A. P. Lee, "Monodispersed microfluidic droplet generation by shear focusing microfluidic device," Sens. Actuators, B **114**(1), 350–356 (2006).
[31]C. N. Baroud, F. Gallaire, and R. Dangla, "Dynamics of microfluidic droplets," Lab Chip **10**(16), 2032–2045 (2010).
[32]X. Gu *et al.*, "Numerical simulation of droplet impacting on a microstructured surface: Geometry, wettability, and control of jump-off force," Phys. Fluids **36**(2), 022025 (2024).
[33]N. Naz and Y. Sui, "A three-dimensional level set method for droplet sorting using a non-uniform electric field," Phys. Fluids **35**(8), 082103 (2023).
[34]Z. Fu *et al.*, "Droplet impact simulation with Cahn–Hilliard phase field method coupling Navier-slip boundary and dynamic contact angle model," Phys. Fluids **36**(4), 042115 (2024).
[35]S. G. Sontti and A. Atta, "CFD analysis of microfluidic droplet formation in non–Newtonian liquid," Chem. Eng. J. **330**, 245–261 (2017).
[36]P. Jangir and A. K. Jana, "CFD simulation of droplet splitting at microfluidic T-junctions in oil–water two-phase flow using conservative level set method," J. Braz. Soc. Mech. Sci. Eng. **41**, 1–16 (2019).
[37]T. Hutter *et al.*, "Formation of spherical and non-spherical eutectic gallium-indium liquid-metal microdroplets in microfluidic channels at room temperature," Adv. Funct. Mater. **22**(12), 2624–2631 (2012).
[38]B. Gol *et al.*, "Continuous transfer of liquid metal droplets across a fluid–fluid interface within an integrated microfluidic chip," Lab Chip **15**(11), 2476–2485 (2015).
[39]L. Tian, M. Gao, and L. Gui, "A microfluidic chip for liquid metal droplet generation and sorting," Micromachines **8**(2), 39 (2017).
[40]X. He *et al.*, "A 3D-printed coaxial microfluidic device approach for generating magnetic liquid metal droplets with large size controllability," Microfluid. Nanofluid. **24**, 1–14 (2020).
[41]M. De Menech, "Modeling of droplet breakup in a microfluidic T-shaped junction with a phase-field model," Phys. Rev. E **73**(3), 031505 (2006).
[42]Z. Liu *et al.*, "Generation of droplets in the T-junction with a constriction microchannel," Microfluid. Nanofluid. **22**, 1–9 (2018).